Onset of necking in electro-magnetically formed rings

Nicolas Triantafyllidis[*], Joshua R. Waldenmyer[1]

Department of Aerospace and Engineering, The University of Michigan, Ann Arbor, MI 48109-2140, USA

Abstract

The electromagnetic forming (EMF) process is an attractive manufacturing technique, which uses electromagnetic (Lorentz) body forces to fabricate metallic parts. One of the many advantages of EMF is the considerable ductility increase observed in several metals, with aluminum featuring prominently among them. The quantitative explanation of this phenomenon is the primary motivation of this work.

To study the ductility increase due to EMF, an aluminum ring is placed outside a fixed coil, which is connected to a capacitor. Upon the capacitor's discharge, the time varying current in the coil induces a larger current in the ring specimen and the resulting Lorentz forces make it expand. The coupled coil–ring electromagnetic and thermomechanical problem is solved, using an experimentally obtained constitutive model for a particular aluminum alloy. Our results show that for realistic imperfections, the EMF ring starts necking at strains about six times larger than its static counterpart, as observed experimentally. This study establishes the importance of solving the fully coupled electromagnetic and thermomechanical problem and provides insight on how different constitutive parameters influence ductility in an EMF process.
© 2004 Elsevier Ltd. All rights reserved.

Keywords: A. Electromechanical processes; A. Thermomechanical processes; B. Finite strain; B. Viscoplastic material; C. Energy methods

1. Introduction

Electromagnetic forming (EMF) is a highly flexible and cost-effective method of implementing high-velocity sheet metal forming. It is typically accomplished by

---

[*] Corresponding author. Tel.: +1-734-763-2356; fax: +1-734-763-0578.
E-mail address: nick@engin.umich.edu (N. Triantafyllidis).
[1] Present address: Mail stop S4027, P.O. Box 179, Denver, CO 80201, USA.

connecting a conducting actuator (usually a solenoid coil made of copper windings) in series with a large capacitor bank charged under high voltage and equipped with fast action switches. By discharging the capacitor bank, the large transient current appearing in the actuator produces by induction strong eddy currents in the nearby metallic workpiece. The presence of these eddy currents inside the magnetic field generated by the currents of the actuator result in Lorentz body forces in the workpiece, which are responsible for its plastic deformation.

The EMF technique was first used in this country in the 1950s and 1960s, due to its advantages in enabling the fabrication of many complex geometry parts and in enhancing the formability of low ductility materials. EMF techniques are popular in the aerospace and automotive industries due to a number of advantages they hold over conventional forming techniques, such as repeatability (because of its electric nature, energy input can be carefully adjusted), non-contact (no lubrication needed and no tool marks to worry about) and speed (typical EMF processes duration is of the order of 10 μs). Of particular interest to the present work is the significant increase in ductility observed in certain EMF metals, with aluminum featuring prominently among them. Experimental results by Balanethiram and Daehn (1992) and Balanethiram and Daehn (1994) have produced forming limit diagrams that show that although a conventionally formed structural steel alloy (DFQ steel) is about twice as ductile as a conventionally formed aluminum one (6061-T4 aluminum), the EMF process can increase the ductility of the same aluminum alloy up to a factor of six. A theoretical explanation of this fact, based on a coupled electromagnetic and thermomechanical modeling of a relevant EMF experiment is the motivation of the present work.

Although research work in EMF during the 1950s and 1960s was important, as evidenced by the (mainly experimental) number of publications reported in the engineering literature, the research activity in the next twenty years (from the early 1970s to the early 1990s) diminished to a trickle (see survey article by Daehn et al., 1999). Even in the heyday of interest on EMF, the scarcity of modeling work for these processes is strikingly noticeable. The main reason can be attributed to timing: computational methods and the hardware required for the execution of the resulting numerical algorithms were not yet in place. Although the physics of these complex thermomechanical plus electromagnetic phenomena were in principle understood, the pertaining coupled non-linear systems of partial differential equations could not be solved with the technology available at that time.

Of the initial modeling efforts in EMF, we mention the work of Furth and Waniek (1956) and Furth and Waniek (1957) who describe the basic equations of the problem as also do the analytical studies of Birdsall et al. (1961) and Meagher (1964). Subsequent work by Al-Hassani et al. (1974) relaxed some of the assumptions in the previous works and calculated numerically the Lorentz forces in the workpiece. As computing power became more readily accessible, a new set of EMF modeling studies has emerged since the 1980s. Of particular interest here is the experimental and theoretical paper by Gourdin (1989) who has studied the electromagnetic expansion of tin, copper and lead rings. Gourdin formulated the coupled electromagnetic and thermomechanical problem by taking into account the geometry changes of the ring to find the correct induced currents. He has assumed several stress–strain laws

for the axisymmetric, uniaxial deformation of the ring but did not model necking or fracture.

The electromagnetically loaded ring expansion and fragmentation problem has also been addressed in the mechanics literature, starting with the experimental investigations of Niordson (1965). Since then, additional experimental (e.g. Grady and Benson, 1983) and theoretical (e.g. Han and Tvergaard, 1995; Pandolfi et al., 1999; Sorensen and Freund, 2000; Becker, 2002) investigations have addressed the mechanical aspects of ring expansion and the ultimate fragmentation process, using 3D modeling of the ring and sophisticated failure criteria. Although not formulated for the ring, the recent work by Mercier and Molinari (2003) addresses the onset of a bifurcation instability and wavelength selection in the dynamic loading of elastoplastic solids under uniaxial extension, thus providing important insight on the influence of inertia and material properties on the failure initiation mechanism for a ring. However these refined mechanics studies of ring expansion ignored the coupled nature of the problem and assumed the velocity boundary conditions imposed on the specimen (known). The common feature that emerges from the survey of the existing literature on EMF is the absence of studies where the coupled electromagnetic and finite strain thermomechanical problem is addressed concurrently with the onset of necking, and this is exactly the approach adopted in the present work.

The formulation of the coupled electromagnetic and thermomechanical problem is presented in Section 2, followed by an onset-of-necking "*band type*" analysis in the spirit of Marciniak and Kuczynski (1967). The numerical results for a ring made from a 6061-T6 aluminum alloy whose constitutive properties have been measured experimentally by Yadav et al. (1995) are given and discussed in Section 3. There among other things it is shown that for the alloy considered and for realistic imperfections, the observed ductility improvement over a purely mechanical process is close to experimental observations. The main reason for the enhanced ductility of the rings, which is discussed in Section 4, lies in the material's rate sensitivity, which is known to delay necking in uniaxial tension tests (see Hutchinson and Neale, 1977). The presentation is concluded by some general observations and suggestions for further investigations, also given in Section 4.

2. Problem formulation

The schematic diagram of the ring expansion experiment is shown in Fig. 1. The setup consists of a capacitor of capacitance C_1 connected to a coil of radius r_1 and placed coaxially and symmetrically inside a ring (also termed the "*specimen*") of a slightly larger initial radius r_0. Here and subsequently, all quantities associated with the coil will be denoted by a subscript (1) while their counterparts for the ring will be denoted by a subscript (2). To avoid unnecessarily cumbersome notation, quantities associated with the ring that do not have a coil counterpart will have no subscript, while a (0) subscript designates the initial value, at $t = 0$, of a ring-associated variable, i.e. $r_0 \equiv r_2(0)$.
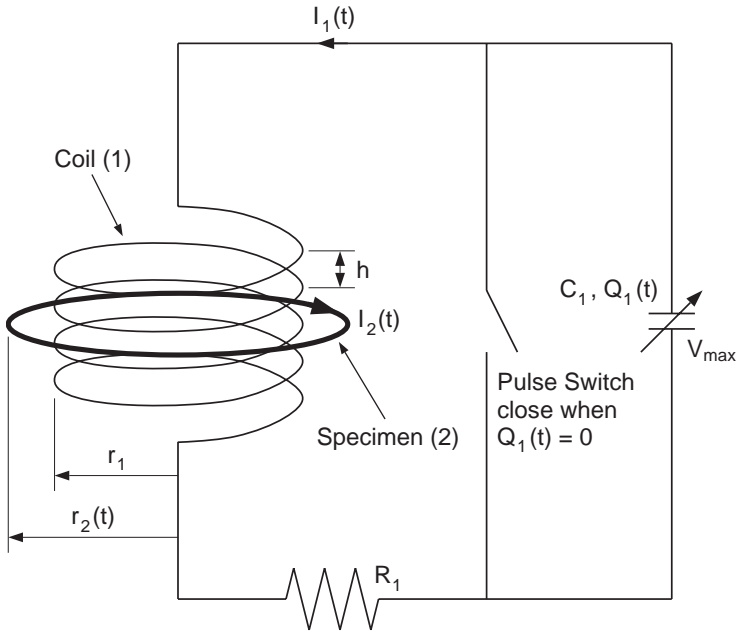
Fig. 1. Schematic representation of the experimental setup for the electromagnetic ring expansion experiment.

By discharging the capacitor connected to the coil, a time-dependent current, $I_1(t)$, flows through it and, according to Lenz's Law, induces in the ring a current, $I_2(t)$, in the opposite direction. The resulting Lorentz force exerted on the ring (since the current I_2 interacts with the coil's magnetic field) is responsible for its expansion. The switch shown in Fig. 1 is used to produce a single pulse in the coil by preventing a sign change in I_1, which would have resulted in an unwanted subsequent contraction of the ring following its initial expansion phase. The section continues with the presentation of the equations governing the electromechanical system at hand and concludes with the derivations pertaining to the onset of necking in the ring.

2.1. Governing equations

The system's governing ordinary differential equations are derived using the principles of classical mechanics for finite degree of freedom systems as follows. First the Lagrangian, $\mathscr{L}$, of the system is constructed as the difference of the generalized kinetic energy, $\mathscr{T}$, and generalized potential energy, $\mathscr{V}$, namely

$$\mathscr{L}(Q_1, Q_2, \varepsilon^p, r_2) \equiv \mathscr{T} - \mathscr{V},$$

$$\mathscr{T} \equiv \tfrac{1}{2} M_2(\dot{r_2})^2 + \tfrac{1}{2} [L_{11}(\dot{Q}_1)^2 + 2L_{12}(r_2)\dot{Q}_1\dot{Q}_2 + L_{22}(r_2)(\dot{Q}_2)^2],$$

$$\mathscr{V} \equiv \frac{1}{2C_1}(Q_1)^2 + \frac{V_2 E}{2}(\varepsilon^e)^2. \tag{2.1}$$

The four degrees of freedom of the system are the electric charges, Q_1 and Q_2, in the coil and the ring, the plastic strain, ε^p, of the ring and the radius, r_2, of the ring, since only axisymmetric deformations are considered. In addition, here and subsequently, a quantity surmounted by a dot denotes the time derivative of the quantity in question.

The generalized kinetic energy of the system, $\mathscr{T}$, consists of a mechanical part (one-half times mass, M_2, times the square of the ring's radial velocity, $v_2 = \dot{r}_2$) plus an electromagnetic part, which is the energy stored in the coil and the ring. This electromagnetic energy is a quadratic function of the currents, $I_1 = \dot{Q}_1$ and $I_2 = \dot{Q}_2$, and depends on L_{11} and $L_{22}(r_2)$, which are, respectively, the self-inductances of the coil and the ring, and on $L_{12}(r_2)$, which is the mutual inductance between the coil and the ring. All inductances depend on geometry and their explicit expressions are given in Appendix A. Attention is here drawn to the fact that the inductances L_{12} and L_{22} depend on the ring's radius, r_2, and hence—in contrast to L_{11}—are time dependent, thus greatly influencing the resulting currents in the system.

The generalized potential energy of the system, $\mathscr{V}$, consists of an electrostatic part (the energy stored in the capacitor equals one-half the square of the capacitor's charge, Q_1, divided by the capacitance, C_1) plus a mechanical part which is the ring's volume, V_2, multiplied by its elastic energy density (one half the ring's Young's modulus, E, times the square of its elastic strain ε^e). The elastic strain is given in terms of the total (logarithmic) strain, ε, the plastic strain, ε^p, and the thermal strain, ε^θ, by

$$\varepsilon^e = \varepsilon - \varepsilon^p - \varepsilon^\theta,$$

$$\varepsilon \equiv \ln(r_2/r_0),$$

$$\varepsilon^\theta \equiv \beta(\theta - \theta_0), \tag{2.2}$$

where β is the ring's thermal expansion coefficient and θ is the ring's temperature, while θ_0 is its initial temperature ($\theta_0 \equiv \theta(0)$). For simplicity, it is further assumed that the ring is incompressible and that its mass density μ is temperature-insensitive. Hence the ring's mass, M_2, and volume, $V_2 = M_2/\mu$, are time-independent constants.

The governing equations for the dissipative system described by the Lagrangian in (2.1) are

$$\frac{\mathrm{d}}{\mathrm{d}t}\left(\frac{\partial \mathscr{L}}{\partial \dot{q}_i}\right) - \frac{\partial \mathscr{L}}{\partial q_i} + f_i = 0 \quad (i = 1,\dots,4), \tag{2.3}$$

where the generalized coordinates, q_i, and their work-conjugate dissipative forces, f_i, are given by

$$q_1 \equiv Q_1, \quad f_1 = R_1 I_1,$$

$$q_2 \equiv Q_2, \quad f_2 = R_2 I_2,$$

$$q_3 \equiv \varepsilon^p, \quad f_3 = V_2 \sigma,$$

$$q_4 \equiv r_2, \quad f_4 = 0. \tag{2.4}$$

The dissipative forces corresponding to Q_1 and Q_2 are the voltage drops due to the ohmic resistances, R_1 and R_2, of the coil and the ring, respectively, while the dissipative force corresponding to ε^p is the axial stress, σ, of the ring multiplied by its volume.

Using the particular form of the system's Lagrangian in Eq. (2.1) in the general expression (2.3), and after taking into account Eqs. (2.2) and (2.4), one obtains the following four equations:

$$i = 1: \quad \frac{d}{dt}(L_{11}\dot{Q}_1 + L_{12}\dot{Q}_2) + \frac{Q_1}{C_1} + R_1\dot{Q}_1 = 0,$$

$$i = 2: \quad \frac{d}{dt}(L_{12}\dot{Q}_1 + L_{22}\dot{Q}_2) + R_2\dot{Q}_2 = 0,$$

$$i = 3: \quad -V_2 E \varepsilon^e + V_2 \sigma = 0,$$

$$i = 4: \quad M_2\ddot{r}_2 - \frac{dL_{12}}{dr_2}\dot{Q}_1\dot{Q}_2 - \frac{1}{2}\frac{dL_{22}}{dr_2}(\dot{Q}_2)^2 + V_2 E \varepsilon^e \frac{1}{r_2} = 0. \tag{2.5}$$

The first two equations are Faraday's Law for the coil and the ring, respectively. The third equation is the stress–elastic strain relation for the ring and the last equation is the ring's equation of radial motion. The above equations could have been obtained by direct considerations (as in Gourdin, 1989), but the present derivation, besides its elegance, is helpful in establishing the system's energy balance, which has not been studied previously to the best of the authors' knowledge.

To establish the system's energy balance one must multiply each one of the four equations in Eq. (2.5) by the corresponding $\dot{q}_i$ and then sum the resulting expressions, obtaining with the help of Eqs. (2.1), (2.2) and (2.4)

$$\sum_{i=1}^{4}\left[\frac{d}{dt}\left(\frac{\partial \mathscr{L}}{\partial \dot{q}_i}\right) - \frac{\partial \mathscr{L}}{\partial q_i}\right]\dot{q}_i = \dot{\mathscr{E}} + \mathscr{D} = 0,$$

$$\mathscr{E} \equiv \mathscr{T} + \mathscr{V},$$

$$\mathscr{D} \equiv \sum_{i=1}^{4} f_i\dot{q}_i. \tag{2.6}$$

Up to this point, no mention of the system's material properties has been made, which are an indispensable ingredient for the solution of the ring expansion problem. For the application of interest, large strains, high strain rates and important temperature increases are expected. Consequently, and given our interest in the ductility increase of EMF formed aluminum, the rate-sensitive, thermoviscoplastic constitutive model in Yadav et al. (2001), which is based on experiments by Yadav et al. (1995) on 6061-T6 Al alloy, is used (in conjunction with Eq. (2.2) and the third equation of Eq. (2.5))

$$\dot{\varepsilon}^p = \begin{cases} \dot{\varepsilon}_0^p\left[\left(\frac{\sigma}{g(\varepsilon^p)}\right)^{1/m} - 1\right] & \text{if } \sigma > g(\varepsilon^p), \\ 0 & \text{if } \sigma \leqslant g(\varepsilon^p), \end{cases}$$

$$g(\varepsilon^p) = \sigma_y\left(1 + \frac{\varepsilon^p}{\varepsilon_0^p}\right)^n\left[1 - \left(\frac{\theta - \theta_0}{\theta_m - \theta_0}\right)^\alpha\right]. \tag{2.7}$$

In the power law type model presented above, m, n and α are the rate-sensitivity, hardening and thermal sensitivity exponents, respectively, while ε_0^p and $\dot{\varepsilon}_0^p$ are the reference plastic strain and plastic strain rate. In addition, θ_m is the material's melting temperature, θ_0 the reference temperature and σ_y the yield stress at θ_0.

It is tacitly assumed (and verified numerically in all the subsequent calculations) that the ring is under loading conditions $\dot{\varepsilon} > 0$ until it reaches its maximum strain, at which point the calculations are terminated, thus justifying the absence of unloading considerations. The material in the ring starts by loading elastically ($\varepsilon^p = 0, \dot{\varepsilon} > 0$) and subsequently enters its plastic range when the strain reaches a (thermally dependent) yield strain, ε_y^θ, given by

$$\varepsilon_y^\theta = \beta(\theta - \theta_0) + \frac{\sigma_y}{E}\left[1 - \left(\frac{\theta - \theta_0}{\theta_m - \theta_0}\right)^\alpha\right], \tag{2.8}$$

which has been obtained by requiring stress continuity at the first onset of yielding.

Similarly to the mechanical properties, the electrical properties of the system's materials are required. Thus if ρ is the (temperature-dependent) resistivity of the ring, its resistance, R_2, is given by

$$R_2 = \rho(\theta)2\pi r_2/a_2,$$
$$\rho(\theta) = \rho_0 + \gamma(\theta - \theta_0), \tag{2.9}$$

where a_2 is the ring's current cross-section, ρ_0 its resistivity at the reference temperature, θ_0, and γ the resistivity's temperature sensitivity (assumed linear). The determination of the current cross-section, a_2, in terms of the current radius of the ring, r_2, and its initial cross-section, a_0, is achieved with the help of the incompressibility assumption, mentioned earlier in this section,

$$V_2 = 2\pi r_2 a_2 = 2\pi r_0 a_0. \tag{2.10}$$

A similar relation to Eq. $(2.9)_1$ is used to calculate the total resistance of the main coil and it is also recorded for completeness in Appendix B.

So far we dispose of four equations, Eq. (2.5) (the third equation from Eq. (2.5) is combined with the kinematics, Eq. (2.2) and constitutive law, Eq. (2.7) for the five unknown quantities: Q_1, Q_2, ε^p, r_2 and θ. Consequently, an additional equation is required for the solution of the problem. This additional equation is obtained by assuming that all the ohmic and part of the plastic energy—given by a factor χ— dissipated in the ring is converted into heat, a reasonable assumption due to the short duration of the ring's expansion phase. Hence

$$M_2 c_p \dot{\theta} = V_2 \chi \sigma \dot{\varepsilon}^p + R_2(I_2)^2, \tag{2.11}$$

where c_p is the ring's specific heat, $V_2 \sigma \dot{\varepsilon}^p$ is the ring's rate of plastic work and $R_2(I_2)^2$ is its ohmic dissipation. The coil's temperature changes are ignored.

At this point, one has five equations for the five unknowns Q_1, Q_2, ε^p, r_2 and θ. To solve the system for these five time-dependent quantities, the appropriate initial

conditions are required. These conditions account for the fact that the system at $t = 0$ is at temperature θ_0 and has no initial velocity or currents, no permanent deformations, a maximum charge in the primary circuit $Q_1 = C_1 V_{\max}$—where $V_{\max}$ is the initial voltage of the capacitor—and no charge in the specimen, i.e.

$$\text{at } t = 0 \quad \begin{cases} Q_1 = C_1 V_{\max}, \ Q_2 = \varepsilon^p = 0, \\ r_2 = r_0, \\ \theta = \theta_0, \\ \dot{Q}_1 = \dot{Q}_2 = \dot{r}_2 = 0. \end{cases} \tag{2.12}$$

The fact that the initial rates of Q_1, Q_2 and r_2 must be prescribed (and not the initial rates of ε^p or θ) is explained by Faraday's Laws, Eq. (2.5)$_1$ and Eq. (2.5)$_2$, and the ring's equation of motion, Eq. (2.5)$_4$, which involve second derivatives of these variables. In contrast, the evolution equation for the internal variable ε^p, Eq. (2.7), and the equation governing the ring's heating in Eq. (2.11) involve only first order time derivatives of ε^p and θ, thus justifying the corresponding initial conditions in Eq. (2.12). The resulting system of ordinary differential equations is solved numerically as explained subsequently.

2.2. Onset of necking

Having established the governing equations for the axisymmetric motion of the ring, attention is focused next on the determination of the critical strain corresponding to the onset of necking in the ring. As explained in the introduction, in the interest of modeling simplicity, a "*band type*" analysis, introduced by Marciniak and Kuczynski (1967), is to be employed here. The main difference of the present analysis with its purely mechanical counterpart used in the study of necking in rate-sensitive bars by Hutchinson and Neale (1977) is the thermomechanical coupling due to ohmic heating.

Consistently with the assumption of a uniaxial stress state in the ring (due to its small curvature, $\sqrt{a_2} \ll r_2$) one assumes the existence of a "*weak*" zone in the ring, see Fig. 2, whose initial cross-section, $a_{\text{in}}(0)$ is slightly inferior to the initial cross-section of the ring, $a_{\text{out}}(0) = a_0$,

$$a_{\text{in}}(0) = (1 - \xi)a_{\text{out}}(0), \quad 0 < \xi \ll 1. \tag{2.13}$$

The (in) and (out) subscripts herein refer to quantities associated with the in(side) and the out(side) of the weak zone of the ring. It is tacitly assumed that the extent of the weak zone is small and that the differences between quantities evaluated inside and outside this zone are so small (up to the onset of necking) as to not affect the axisymmetric solution of the ring. Consequently, the solution to the system of ordinary differential equations (2.5) and (2.11) with initial conditions (2.12) will be subsequently labeled with a subscript (out) since it provides all the quantities outside the weak zone.

As the loading process starts, the strains inside and outside the weak zone are almost the same ($\varepsilon_{\text{in}}/\varepsilon_{\text{out}} = 1 + \mathcal{O}(\xi)$). With the continuation of the loading process there comes a time that the strain ratio $\varepsilon_{\text{in}}/\varepsilon_{\text{out}}$ starts increasing very rapidly and without bound, as seen in Fig. 2. The onset of necking strain, $\varepsilon_{\text{neck}}$, is defined at the strain $\varepsilon_{\text{out}}(t_{\text{neck}})$,
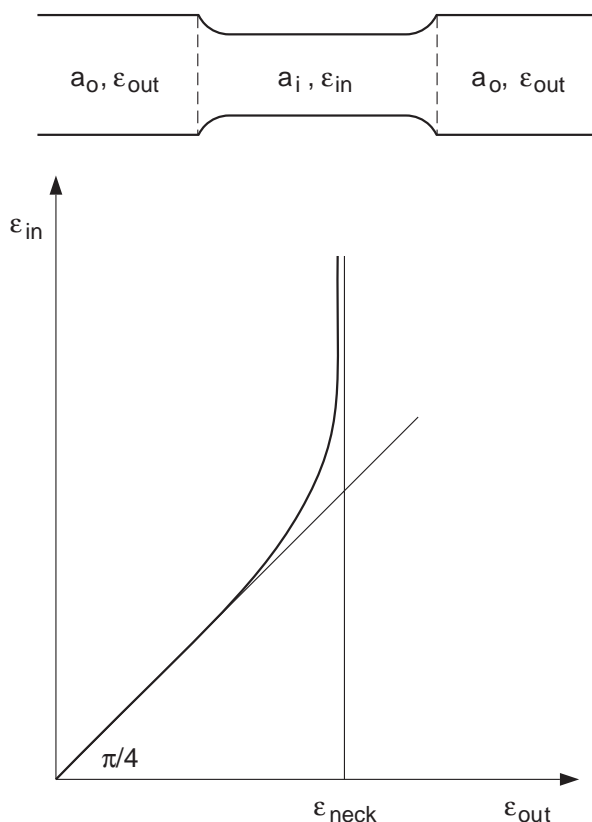
Fig. 2. Evolution of strain inside and outside a "weak" zone of the ring.

where t_{neck} is the time at which $\varepsilon_{in}/\varepsilon_{out}$ exceeds a certain value (which in all subsequent calculations is taken to be equal to four). A higher than four value for the definition of the onset of necking makes practically no difference for the value found for ε_{neck}, although it requires much smaller step sizes near t_{neck} due to the practically vertical asymptote of $\varepsilon_{in}(t)/\varepsilon_{out}(t)$ near t_{neck}. The numerical calculation of $\varepsilon_{in}(t)$ is based on the assumption of force and current continuity across the two zones of the ring, in addition to the constitutive, heat and incompressibility equations for the material, and works as follows: the force and current continuity conditions between the zones are

$$\sigma_{in}a_{in} = \sigma_{out}a_{out}, \quad \text{(force continuity)},$$

$$(I_2)_{in} = (I_2)_{out}, \quad \text{(current continuity)}. \tag{2.14}$$

The incompressibility condition, Eq. (2.10), in conjunction with the logarithmic strain definition $(2.2)_2$ and the definition of the imperfection in Eq. (2.13) yields

$$a_{in} = a_{out}(1 - \xi)\exp(\varepsilon_{out} - \varepsilon_{in}). \tag{2.15}$$

By combining Eqs. (2.14) and (2.15) with the rate form of the elastic stress definition, Eqs. (2.5)$_3$ and (2.2), one obtains

$$\dot{\varepsilon}_{in} = \frac{\dot{\varepsilon}_{in}^{p} + \beta\dot{\theta}_{in} + [\exp(\varepsilon_{in} - \varepsilon_{out})/E(1 - \xi)][\dot{\sigma}_{out} - \sigma_{out}\dot{\varepsilon}_{out}]}{1 - [\sigma_{out}/E(1 - \xi)]\exp(\varepsilon_{in} - \varepsilon_{out})}. \tag{2.16}$$

The expressions for $\dot{\varepsilon}_{in}^{p}$ and $\dot{\theta}_{in}$ are found next in terms of ε_{in}^{p}, ε_{in}, θ_{in} and the known solution for the ring. From the definition of the plastic strain in Eq. (2.7), and assuming that we are in the plastic zone, and combining with force continuity (2.14) and (2.15), one has

$$\dot{\varepsilon}_{in}^{p} = \dot{\varepsilon}_{0}^{p} \left[\left(\frac{\sigma_{out}\exp(\varepsilon_{out} - \varepsilon_{in})/(1 - \xi)}{\sigma_{y}(1 + \varepsilon_{in}^{p}/\varepsilon_{0}^{p})^n[1 - ((\theta_{in} - \theta_0)/(\theta_m - \theta_0))^\alpha]} \right)^{1/m} - 1 \right]. \tag{2.17}$$

The expression for $\dot{\theta}_{in}$ is obtained with the help of the heat equation, Eq. (2.11), the force and current continuity, Eqs. (2.14) and (2.15) and reads

$$\dot{\theta}_{in} = \left(\frac{\rho(\theta_{in})}{\rho(\theta_{out})} \right) \left(\frac{\exp(2\varepsilon_{in} - 2\varepsilon_{out})}{(1 - \xi)^2} \right) \left(\frac{\mu c_{p}(\theta_{out})\dot{\theta}_{out} - \sigma_{out}\dot{\varepsilon}_{out}^{p}}{\mu c_{p}(\theta_{in})} \right)$$
$$+ \left(\frac{\sigma_{out}\dot{\varepsilon}_{in}^{p}}{\mu c_{p}(\theta_{in})} \right) \left(\frac{\exp(\varepsilon_{out} - \varepsilon_{in})}{1 - \xi} \right). \tag{2.18}$$

By substituting Eq. (2.17) into Eq. (2.18) and both into Eq. (2.16) one obtains a first-order system of ordinary differential equations for $\varepsilon_{in}, \varepsilon_{in}^{p}, \theta_{in}$,

$$\dot{\mathbf{x}}_{in} = \mathbf{f}(\mathbf{x}_{in}, \dot{\mathbf{x}}_{out}, \mathbf{x}_{out}) \quad \mathbf{x} \equiv (\varepsilon, \varepsilon^{p}, \theta), \tag{2.19}$$

which is solved numerically using a fourth-order Runge–Kutta algorithm.

3. Results

For all the numerical calculations reported here, the geometric and electrical properties of the main circuit are those used in the experimental setup of Gourdin (1989), while the ring specimen is a 6061-T6 Al alloy whose experimentally measured mechanical properties are given in Yadav et al. (2001). For reasons of completeness of the presentation, all the geometric, electrical and mechanical properties of the main circuit and of the base case specimen are given in Appendix B. For the same reason, the calculation of the self-inductances of the coil L_{11} and specimen L_{22} and of the coil –specimen mutual inductance L_{12} are also included in Appendix A.

The results are presented in dimensionless form and the definitions of the necessary characteristic quantities are given in this section as the need arises. The first such constant introduced is the characteristic time t_0, which is the time required for the current in the coil circuit to reach its first maximum—in the absence of the specimen ring. Hence t_0 is the quarter period of a simple LRC circuit with inductance L_{11}, resistance
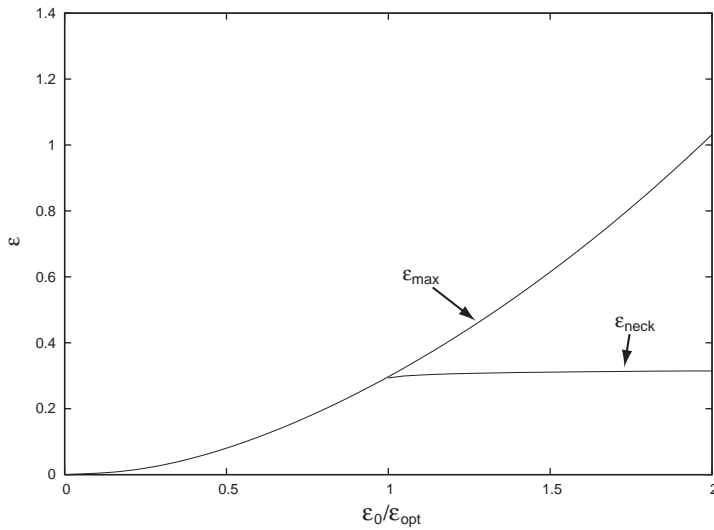
Fig. 3. Maximum and onset-of-necking strains as a function of the energy stored in the capacitor ($\mathscr{E}_{\text{opt}}$ is energy at which max and onset-of-necking strains for base case specimen coincide).

R_1 and capacitance C_1, and is given by

$$t_0 \equiv \frac{\pi}{2} \left[\frac{1}{L_{11} C_1} - \left(\frac{R_1}{2 L_{11}} \right)^2 \right]^{-1/2}. \tag{3.1}$$

As an indication, we mention that for the base case, $t_0 = 12.4\ \mu\text{s}$ (see Eq. (B.3)).

The numerical solutions of the governing system of ODEs given in Section 2 is achieved through a fourth order Runge–Kutta algorithm with a step size $\Delta t = 10^{-3} t_0$. The accuracy of the algorithm and the size of the step are determined by comparing the numerical results to the analytical solution of the linearized coil/ring system. In this analytical solution the ring is assumed to be linearly elastic and its strains small, so as to neglect the change of the inductances. An additional check of the accuracy of the algorithm for the actual non-linear system of ODEs is based on the verification, at all times t, of the energy balance equation which from Eq. (2.6) reads

$$\mathscr{E}_0 = \mathscr{E}(t) + \int_0^t \mathscr{D}\, \mathrm{d}t \quad \mathscr{E}_0 \equiv \mathscr{E}(0). \tag{3.2}$$

The dependence of the maximum $\varepsilon_{\max}$ and necking $\varepsilon_{\text{neck}}$ strains for the base case of a 6061-T6 Al ring as a function of the energy stored in the capacitor $\mathscr{E}_0 (= 0.5 C_1 V_{\max}^2)$ is depicted in Fig. 3. The energy is non-dimensionalized by using the optimal energy $\mathscr{E}_{\text{opt}}$ defined as the energy stored in the capacitor for which the base case Al ring (with an imperfection $\xi = 10^{-3}$) starts necking at maximum strain (i.e. $\varepsilon_{\max} = \varepsilon_{\text{neck}}$). For the base case this energy is found to be $\mathscr{E}_{\text{opt}} = 545.6$ J and corresponds to an initial voltage of
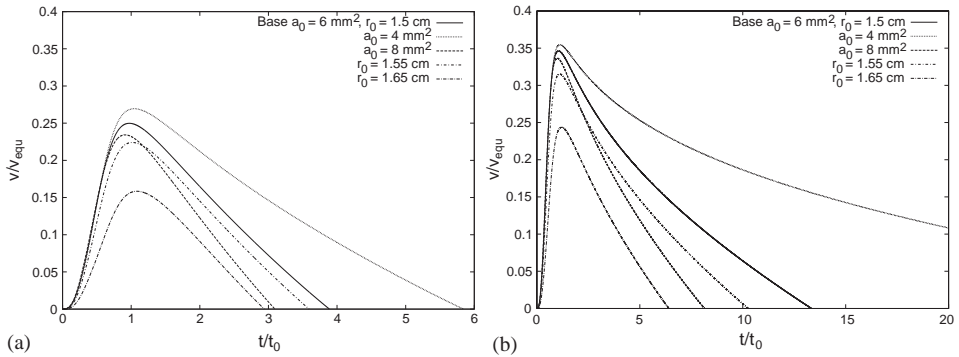
Fig. 4. Dimensionless velocity versus dimensionless time for different initial radii, r_0, and cross-sections, a_0, of the specimen (a) for $\mathscr{E} = \mathscr{E}_{\mathrm{opt}}$ and (b) for $\mathscr{E} = 2\mathscr{E}_{\mathrm{opt}}$.

$V_{\max} = 4.4 \times 10^3$ V (see Eq. (B.3)). For higher energies stored in the capacitor notice that the necking strain remains practically unchanged, while the maximum strain that the ring would have attained had the deformation remained axisymmetric (physically impossible—maximum strain results are shown here just for comparison purposes) increases dramatically. For capacitor energies $\mathscr{E}_0 < \mathscr{E}_{\mathrm{opt}}$ the ductility of the ring is not exhausted, since no necking is found during the axisymmetric expansion of the ring from its stress-free configuration all the way up to its maximum strain.

The time evolution of the ring velocity is depicted in Fig. 4a and b for capacitor energies $\mathscr{E}_{\mathrm{opt}}$ and $2\mathscr{E}_{\mathrm{opt}}$, respectively. The ring's velocity is non-dimensionalized with respect to the corresponding equivalent initial velocity v_{equ}, which is defined as the initial velocity of the ring had all the energy stored in the capacitor been available as kinetic energy at the onset of the deformation process, i.e.

$$\tfrac{1}{2} M_2 v_{\mathrm{equ}}^2 = \tfrac{1}{2} C_1 V_{\max}^2 \equiv \mathscr{E}_0. \tag{3.3}$$

For the base case, this characteristic velocity is found to be $v_{\mathrm{equ}} = 845.37$ m/s (see Eq. (B.3)).

Since the ring expansion process starts at rest, the initial velocity is zero. Moreover, because initially the currents, and hence the Lorentz forces are zero, the initial acceleration is also zero, thus explaining the horizontal tangent of the velocity graphs in Fig. 4. Due to the important ohmic and plastic work dissipation of the EMF process, the maximum velocity is always considerably less than the equivalent initial velocity. For a given capacitor energy, both the maximum velocity and the time it takes to reach the maximum strain decrease as the ring's cross-section increases, due to the increased amount of material that is deformed with the same energy—compare the curves for $a_0 = 4$, 6 and 8 mm, respectively. Also for a given energy the maximum velocity and the time it takes to reach the maximum strain decrease for increasing radius of the ring, due to the strong decay of the magnetic field outside the coil as the distance from the coil's axis increases—compare the curves for $r_0 = 1.50$, 1.55 and 1.65 cm.
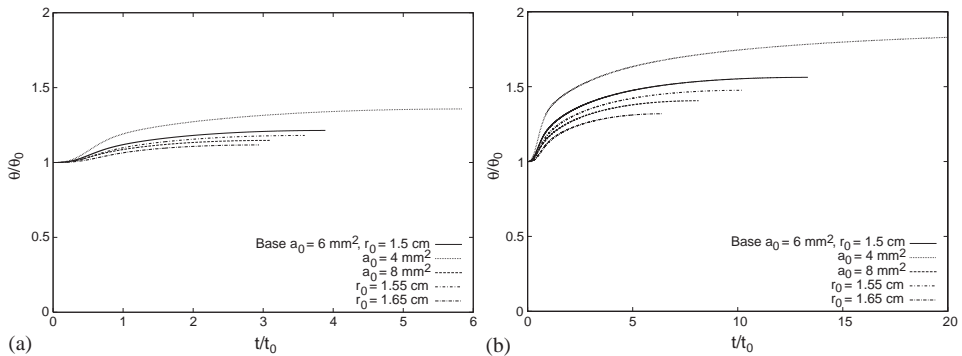
Fig. 5. Dimensionless temperatures versus dimensionless time for different initial radii, r_0, and cross-sections, a_0, of the specimen (a) for $\mathscr{E} = \mathscr{E}_{opt}$ and (b) for $\mathscr{E} = 2\mathscr{E}_{opt}$.

By doubling the energy in the capacitor, the same ring reaches a higher maximum velocity and takes a considerably longer time to reach its maximum strain, which can be seen by a direct comparison of the two groups of velocity graphs in Fig. 4 (for this case the equivalent initial velocity increases from 845.37 to 1195.53 m/s, see remark after Eq. (B.3)). Notice also the change of shape in these velocity graphs since the velocity peak is reached at about $t = t_0$—independently of the initial energy of the capacitor—while the time that the ring requires to reach its maximum strain (i.e. the $v = 0$ point in the graphs) increases considerably with the increasing initial energy stored in the capacitor.

The evolution of the ring's dimensionless temperature θ/θ_0 versus the dimensionless time t/t_0 is depicted in Fig. 5a and b for initial capacitor energies $\mathscr{E}_{opt}$ and $2\mathscr{E}_{opt}$, respectively. The geometries of the rings are the same as the ones presented in Fig. 4. Notice that an increase of the ring's cross-section leads to a decrease in its temperature due to the drop of the ring's resistance (recall that the ohmic dissipation in the specimen, which is proportional to its resistance, is converted to heat). Also an increase in the radius of the ring results in lower temperatures (assuming again the same initial energy of the capacitor) due to the weaker magnetic fields experienced by the larger radius rings. As expected, when the same ring is subjected to the discharge of a capacitor with double the initial energy, the higher induced currents result in higher ohmic dissipation and hence an increase in the temperature of the ring, as evidenced by the comparison between rings with the same geometry in the two groups of the temperature graphs in Fig. 5.

The graphs of the dimensionless currents I_1/I_0 of the coil and I_2/I_0 of the ring versus the dimensionless time t/t_0 are depicted in Fig. 6a and b for initial capacitor energies $\mathscr{E}_{opt}$ and $2\mathscr{E}_{opt}$, respectively. The characteristic current I_0 is defined as the amplitude of the current in a simple LRC circuit with inductance L_{11}, resistance R_1 and capacitance C_1, and is given by

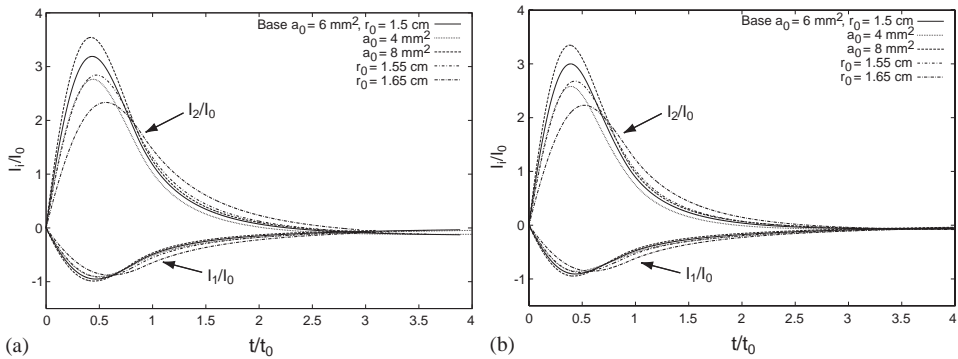$$I_0 \equiv \frac{2}{\pi} \frac{V_{\max} t_0}{L_{11}}, \tag{3.4}$$

Fig. 6. Dimensionless currents versus dimensionless time for different initial radii, r_0, and cross-sections, a_0, of the specimen (a) for $\mathscr{E} = \mathscr{E}_{\mathrm{opt}}$ and (b) for $\mathscr{E} = 2\mathscr{E}_{\mathrm{opt}}$.

where the characteristic time t_0 is defined in Eq. (3.1). For the base case at optimal energy, the characteristic current is $I_0 = 32.6 \times 10^3$ A (see Eq. (B.3)).

It is worth noticing that the initial energy of the capacitor has a rather small effect on the dimensionless currents. On the other hand, an increase in the cross-section of the ring results in an increased current while an increased ring radius leads to lower currents, due to the decay of the coil's outside magnetic field away from its symmetry axis. The change of the ring's cross-sectional area affects the amplitude, but not the shape, of the currents graphs. In contrast, the change of the ring's radius tends to widen the current pulse, in addition to lowering its peak. It should also be mentioned at this point that the current peaks occur at about half the characteristic time, i.e. in half the time as compared to the corresponding peak that would have occurred in the coil in the absence of the ring.

The repartition of the different energies of the system (energy stored in the capacitor, in the coils—primary plus ring—elastic and kinetic energy of the ring) as functions of the dimensionless time is depicted in Fig. 7a while the different dissipations accumulated up to time t (ohmic in coil and ring, plastic dissipation in ring as well as the total dissipation) are plotted versus the dimensionless time in Fig. 7b. The results in Fig. 7 correspond to the base case with an initial capacitor energy $\mathscr{E}_{\mathrm{opt}} = 545.6$ J. Notice in Fig. 7a that the electromagnetic energy stored in the coils peaks at the same time as the currents (recall from Eq. (2.1) that the electromagnetic energy of the coils is a quadratic function of the currents), while the kinetic energy peaks at the time corresponding to the ring's maximum velocity (see Fig. 4a). It is also worth mentioning that the elastic (reversible) energy stored in the ring is negligible.

The energy dissipation results for the base case shown in Fig. 7b show that eventually more than 80 percent of the total available energy is dissipated through the ohmic losses in the coil, while the remainder goes to ohmic losses and plastic work in the ring. Initially, the ohmic losses in the ring are higher due to the rapid increase of the ring current, but as the deformation proceeds the currents die out, while the stresses
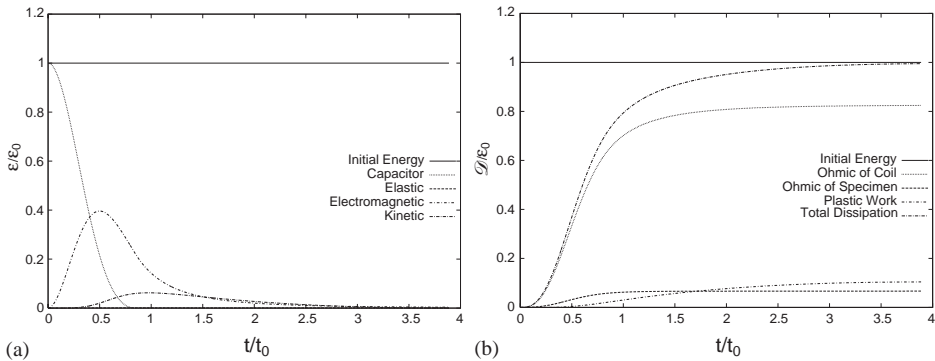
Fig. 7. Partition of (a) energies and (b) dissipations as a function of dimensionless time for the base case experiment at $\mathscr{E}_{\mathrm{opt}}$.

and plastic strains increase to the point that the total plastic work exceeds the ohmic losses in the ring by about half, as seen in Fig. 7b. The sum of all dissipated energies approaches asymptotically the initial energy stored in the capacitor, thus providing an independent accuracy check for the numerical solution procedure.

The influence of the material properties of the ring on its maximum and necking strains as functions of the initial energy of the capacitor is depicted in Fig. 8. In each group of graphs, all geometric and material properties are kept the same to the base case, save for the hardening exponent n which varies in Fig. 8a, the rate sensitivity exponent m which varies in Fig. 8b and the temperature sensitivity exponent α which varies in Fig. 8c. According to Fig. 8a, an increase in the hardening exponent stiffens the material which consequently reaches a lower maximum strain for a given initial energy of the capacitor. In contrast to the maximum strain, the onset of necking strain in the ring increases with increasing hardening, as expected by the higher stiffness of the material. Similar trends are observed in the study of the influence of the rate sensitivity, recorded in Fig. 8b. Observe that an increase in m results in a more viscous —and hence stiffer—material, thus explaining the lowering of the maximum strain for a given initial energy of the capacitor as the rate sensitivity of the ring increases. In contrast to the influence on the maximum strain, an increased rate sensitivity results in delaying the onset of necking, as evidenced by the significant increases in the onset-of-necking strains over the range of m considered in Fig. 8b. In the absence of ohmic effects, our analysis for the necking delay of the rate-sensitive ring reduces to the one given by Hutchinson and Neale (1977) for the uniaxially strained bar. Finally, the influence of the temperature sensitivity exponent depicted in Fig. 8c shows that as α decreases the maximum strain for a given initial energy of the capacitor increases, as expected from the increased thermal softening of the ring. On the other hand, for the range of the temperature sensitivity parameters considered, their influence on the onset-of-necking strains is negligible.

The results in Fig. 8b elucidate better than any others the main physical reason for the increased ductility of EMF rings. In contrast to the small influence of changing
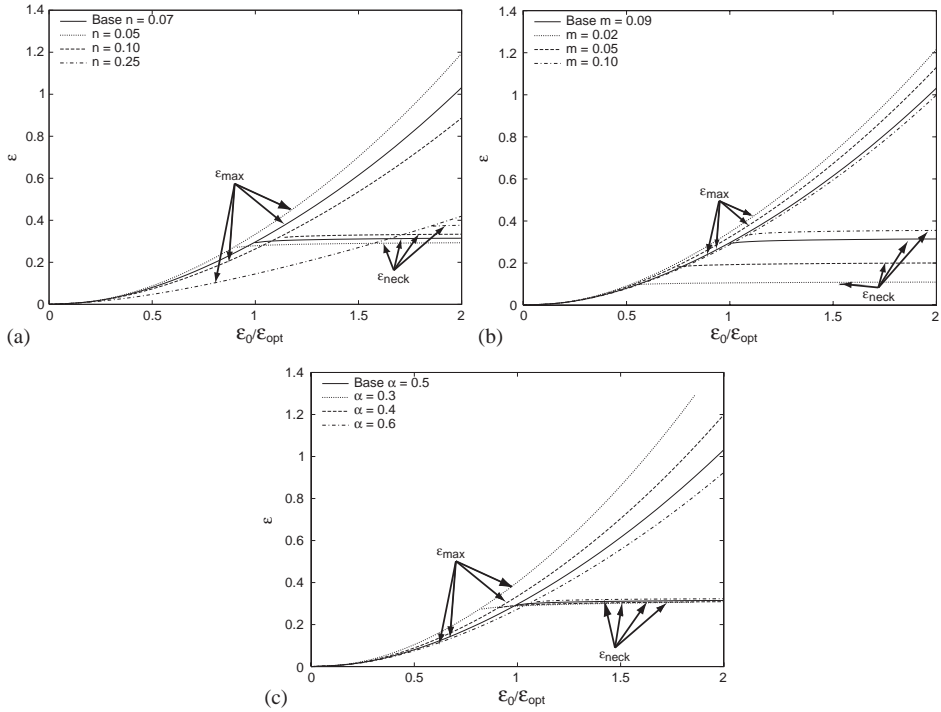
Fig. 8. Influence of constitutive properties on the maximum and onset-of-necking strains (a) for different hardening, (b) for different rate sensitivity and (c) for different temperature sensitivity.

the material's strain hardening or thermal sensitivity, small variations in the rate sensitivity have considerable effects in delaying necking. Of course for rate sensitivity to play an important role, high strain rates have to be encountered during the expansion process. As an indication of the strain rates achieved, we note that for the base case the maximum strain rate during the expansion is of the order $\dot{\varepsilon}_{max} = 1.3 \times 10^4 \text{ s}^{-1}$ (see Eq. (B.3)).

The considerable improvement, as compared to the purely mechanical methods, in the ductility of the electromagnetically formed Al is quantified in Fig. 9. This figure shows the "*ductility improvement ratio*"—defined as the ratio of the onset-of-necking strain in the EMF experiment ε_{emf} over its counterpart in a quasistatic and purely mechanical process ε_{stat}—versus the initial energy stored in the capacitor. The calculation of ε_{stat} is based on the rate and temperature independent behavior of the 6061-T6 Al ring and consists of finding the strain corresponding to the maximum force σa—where a is the current cross-sectional area that can be related to its initial counterpart A by the incompressibility relation $a = A \exp(-\varepsilon)$—in a uniaxial experiment involving this alloy, when the influence of the ring's curvature is ignored. The calculation of ε_{stat}, which is independent of the imperfection amplitude parameter ξ is based on the solution of the
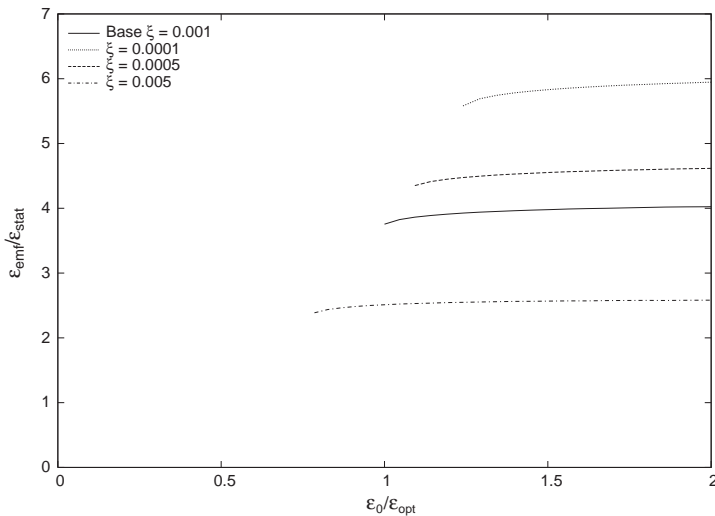
Fig. 9. Ductility enhancement (electromagnetic over static onset-of-necking strains) as a function of capacitor energy for different size imperfections.

following non-linear system:

$$\left(\frac{d(\sigma a)}{d\varepsilon}\right)_{\varepsilon_{stat}} = 0, \quad \sigma = \sigma_y(1 + \varepsilon^p/\varepsilon_0^p)^n, \quad \varepsilon = \varepsilon^p + \sigma/E. \tag{3.5}$$

For reference purpose, we note that $\varepsilon_{stat} = 0.0782$ for the base case (see Eq. (B.3)).

The ductility improvement ratio is very sensitive to the ring's imperfection amplitude parameter ξ, but practically insensitive to the initial energy stored in the capacitor. Notice that by varying ξ from 5×10^{-3} to 10^{-4}, the ductility improvement goes from a factor of 2.5 to about 6, thus explaining the experimentally observed considerable increase in the necking strains of electromagnetically formed Al reported by Balanethiram and Daehn (1992) and Balanethiram and Daehn (1994).

A frequently used simplification in calculating the ductility of expanding rings is to treat the problem as a purely mechanical one which starts deforming from its stress-free configuration under a given initial velocity. To assess the importance of the exact deformation history in the ring ductility calculations, Fig. 10 compares the ductility improvement ratio calculated first on the basis of the exact coupled electromagnetic/thermomechanical process and second based on the simplifying assumption of a purely thermomechanical process which starts with the velocity v_{equ} defined in Eq. (3.3) but which has no electrical currents and hence no Lorentz forces. It is worth pointing out that in spite of the fact that the EMF process proceeds under lower velocities than its purely thermomechanical counterpart (see the EMF velocity profile in Fig. 4), it results in higher onset-of-necking strains, due to higher strain rates. Consequently, the results in Fig. 10 emphasize the importance of solving the exact coupled
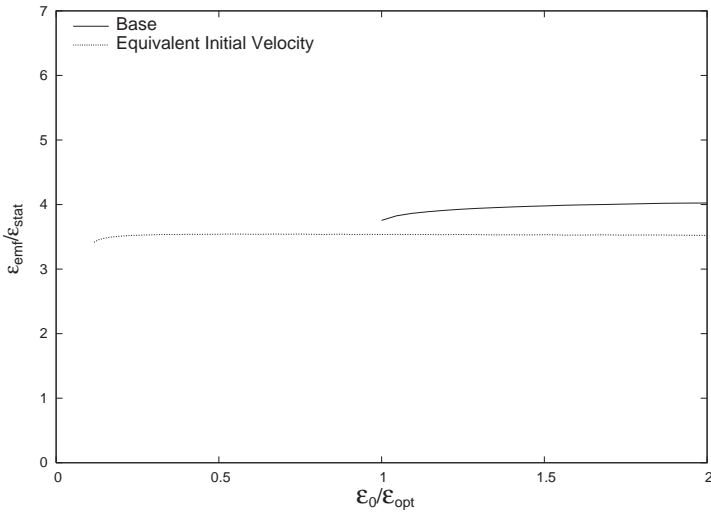
Fig. 10. Ductility enhancement for base EMF case compared to a purely mechanical, initial velocity expansion experiment (i.e. all energy of capacitor is converted to initial mechanical energy).

electromagnetic/thermomechanical problem to accurately predict the onset-of-necking strain in the ring.

4. Conclusion

The work presented here is motivated by the need to quantify the experimentally observed ductility increase (over a quasistatic mechanical method) in electromagnetically formed aluminum alloys. Recognizing the importance of the interaction between the electromagnetic and the thermomechanical effects for the correct determination of the strain history, we solve here the coupled problem of finite strain deformation of a rate and temperature sensitive elastoviscoplastic ring subjected to induced electric currents generated by a coil connected to a capacitor bank. The ductility limit is modeled for simplicity as the onset-of-necking in the uniaxially stressed and axisymmetrically deforming ring under the assumptions (i) of the existence of an imperfection in the form of a thinner section (weak zone) and (ii) of a negligible curvature influence on the necking initiation. The constitutive description for the ring used in the calculations has been obtained experimentally (and independently) for an Al alloy (6061-T6) subjected to strains, strain rates and temperature ranges of the magnitudes encountered in this application.

For realistic magnitudes of the imperfection, our calculations show that the ductility enhancement of the Al ring, when an EMF process is used instead of a mechanical method, can increase six times, in agreement with experimental observations. The main reason for this enhancement can be found in the rate sensitivity of the material and the high strain rates encountered in the EMF process, of the order of 10^4 s^{-1}. Our

calculations show the necessity of modeling the exact deformation history of the ring, which in turn requires the solution of the fully coupled, highly non-linear electromagnetic and thermomechanical set of equations. The reason is that changes in geometry strongly affect the currents which determine the Lorentz forces that in turn give the strain rates and also the temperatures due to the inevitable and important ohmic losses.

The strong dependence of the ductility results on the size of the ring's imperfection is due to our use of a simple "*band type*" analysis to model the onset-of-necking. To obtain ductility results that are insensitive to imperfections, one will have to consider a more sophisticated analysis in which the onset-of-necking is signaled by the appearance of a non-axisymmetric bifurcated solution which will lead to thinning in one part of the ring and eventually end up as a necking failure. Such considerations require at least a two-dimensional description of the EMF process and are envisioned for subsequent investigations. In spite of the fact that the EMF method is known to be an efficient manufacturing technique, it is only recently that it has attracted the attention of the mechanics community. The present work, although relatively simple from a purely mechanics modeling standpoint, is a useful first step to understand the salient features of this coupled electromagnetic/mechanical process.

Acknowledgements

Appendix A. Calculation of inductances

Although well known, the expressions for the self L_{11}, L_{22} and mutual L_{12} inductances are given here for reasons of completeness of the presentation. At the basis of these calculations are two fundamental results, (i) the mutual inductance of two coaxial rings and (ii) the self inductance of a ring with circular cross-section. The self inductance of the main coil L_{11} and the mutual inductance L_{12} between the main coil and the ring are subsequently obtained from these results using superposition.

The mutual inductance $l_m(a, b, z)$ of two coaxial rings of radii a and b respectively, whose parallel planes are separated by a vertical distance z is

$$l_m(a, b, z) = 2\mu_0 \sqrt{ab}[(1 - k^2/2)K(k) - E(k)]/k,$$

$$k^2 \equiv 4ab/[(a + b)^2 + z^2],$$

$$E(k) \equiv \int_0^{\pi/2} (1 - k^2 \sin^2 x)^{1/2} \, dx,$$

$$K(k) \equiv \int_0^{\pi/2} (1 - k^2 \sin^2 x)^{-1/2} \, \mathrm{d}x, \tag{A.1}$$

where μ_0 is the magnetic permeability of vacuum. The calculation of the elliptic integrals $E(k)$ and $K(k)$ is performed numerically.

The self-inductance l_s of a thin circular ring with radius r and radius of cross-section c is given by

$$l_s = \mu_0 \, r[\ln(8r/c) - 7/4]. \tag{A.2}$$

Consequently, the self-inductance of the main coil which consists of N_1 coaxial interacting rings, each with radius r_1, cross-sectional area a_1, radius c_1 and spaced at h_1 apart, is calculated by summing all possible mutual inductances between the N_1 rings and adding their self-inductances, i.e.

$$L_{11} = \sum_{i,j=1; i \neq j}^{N_1} l_m(r_1, r_1, |i - j|h_1) + N_1 l_s(r_1, c_1), \quad c_1 = \sqrt{a_1/\pi}. \tag{A.3}$$

The mutual inductance between coil and ring L_{12} is obtained by summing all the mutual inductances between the radius r_2 specimen ring (placed symmetrically between the rings of the coil) and the N_1 coaxial rings of the coil, i.e.

$$L_{12} = \sum_{i=1}^{N_1} l_m(r_1, r_2, |i - (N_1 + 1)/2|h_1). \tag{A.4}$$

The self-inductance of the specimen ring with radius r_2 and cross-sectional area a_2 and radius c_2 is given by

$$L_{22} = l_s(r_2, c_2), \quad c_2 = \sqrt{a_2/\pi}. \tag{A.5}$$

A derivation of the above expressions for the inductances can be found in any standard book on electromagnetics.

Appendix B. Parameters used in calculations

The following material and geometric parameters have been used in the numerical calculations presented below. The first set of parameters pertains to the main coil:

turns in coil $N_1 = 6$,

radius of coil $r_1 = 1.41 \times 10^{-2}$ m,

spacing of coil turns $h_1 = 2.3 \times 10^{-3}$ m,

sectional area of coil wire $a_1 = 0.8235 \times 10^{-6}$ m^2,

capacitance of main circuit $C_1 = 56.36 \times 10^{-6}$ F,

resistor of main circuit $R_1^* = 0.0425$ Ω,

resistivity of coil wire $\quad \rho_1 = 1.7 \times 10^{-8} \ \Omega$ m,

total resistance of main circuit $\quad R_1 = R_1^* + 2\pi\rho_1 N_1 r_1/a_1.$ (B.1)

The second set of parameters pertains to the properties of the 6061-T6 Al ring:

initial ring radius $\quad r_0 = 1.5 \times 10^{-2}$ m,

initial sectional area of ring $\quad a_0 = 6 \times 10^{-6}$ m^2,

hardening exponent $\quad n = 0.0741,$

rate sensitivity $\quad m = 0.087,$

thermal sensitivity $\quad \alpha = 0.5,$

reference plastic strain $\quad \varepsilon_0^{\mathrm{p}} = 10^{-3},$

reference plastic strain rate $\quad \dot{\varepsilon}_0^{\mathrm{p}} = 10^3,$

Young's modulus $\quad E = 69 \times 10^9$ Pa,

yield stress $\quad \sigma_{\mathrm{y}} = 276 \times 10^6$ Pa,

mass density $\quad \mu = 2.7 \times 10^3$ kg/m^3,

thermal expansion coefficient $\quad \beta = 2.3 \times 10^{-5}$/K,

reference temperature $\quad \theta_0 = 298$ K,

melting temperature $\quad \theta_m = 853$ K,

reference resistivity $\quad \rho_0 = 2.65 \times 10^{-8} \ \Omega$ m,

temp. sensitivity of resistivity $\quad \gamma = 0.0039$/K,

specific heat $\quad c_{\mathrm{p}} = 896$ J/kg K,

plastic work conversion factor $\quad \chi = 0.9.$ (B.2)

Results in this paper are presented in dimensionless form. The values of the characteristic constants employed are obtained for the base case and are:

characteristic time $\quad t_0 = 1.24 \times 10^{-5}$ s,

optimal energy $\quad \mathscr{E}_{\mathrm{opt}} = 545.6$ J,

optimal initial voltage $\quad V_{\mathrm{max}} = 4.4 \times 10^3$ V,

equivalent velocity $\quad v_{\mathrm{equ}} = 845.37$ m/s,

characteristic current $\quad I_0 = 32.6 \times 10^3$ A,

static necking strain $\quad \varepsilon_{\mathrm{stat}} = 0.0782,$

maximum strain rate encountered $\quad \dot{\varepsilon}_{\mathrm{max}} = 1.3 \times 10^4 \ \mathrm{s}^{-1}.$ (B.3)

For the cases calculated with an initial energy $2\mathscr{E}_{\mathrm{opt}}$, the characteristic time t_0 remains the same, the characteristic current I_0 and equivalent velocity v_{equ} should be multiplied by $\sqrt{2}$ while the corresponding maximum strain rate is almost double $\dot{\varepsilon}_{\mathrm{max}} = 2.35 \times 10^4 \ \mathrm{s}^{-1}$.

References

Al-Hassani, S.T.S., Duncan, J.L., Johnson, W., 1974. On the parameters of the magnetic forming process. J. Mech. Eng. Sci. 16, 1.

Balanethiram, V.S., Daehn, G.S., 1992. Enhanced formability of interstitial free iron at high strain rates. Scr. Met. Mater. 27, 1783–1789.

Balanethiram, V.S., Daehn, G.S., 1994. Hyperplasticity-increased forming limits at high workpiece velocities. Scr. Met. Mater. 31, 515–520.

Becker, E., 2002. Ring fragmentation predictions using the Gurson model with material stability conditions and failure criteria. Int. J. Solids Struct. 39, 3555–3580.

Birdsall, D.H., et al., 1961. Magnetic forming. Am. Mach. Metalwork. Manuf. 105, 117.

Daehn, G.S., Vohnout, V.J., DuBois, L., 1999. Improved formability with electromagnetic forming: fundamentals and a practical example. TMS Sheet Metal Forming Symposium, San Diego, February 1999.

Furth, H.P., Waniek, R., 1956. Production and use of high magnetic fields I. Rev. Sci. Instr. 27, 195.

Furth, H.P., Waniek, R., 1957. Production and use of high magnetic fields II. Rev. Sci. Instr. 28, 949.

Gourdin, W.H., 1989. Analysis and assessment of electromagnetic ring expansion at a high-strain-rate test. J. Appl. Phys. 65, 411.

Grady, D.E., Benson, D.A., 1983. Fragmentation of metal rings by electromagnetic loading. Exp. Mech. 23, 93–400.

Han, J., Tvergaard, V., 1995. Effect of inertia on the necking as precursor to dynamic fracture. Eur. J. Mech. A/Solids 14, 287–307.

Hutchinson, J.W., Neale, K.W., 1977. Influence of strain-rate sensitivity on necking under uniaxial tension. Acta Met. 25, 839–846.

Marciniak, Z., Kuczynski, K., 1967. Limit strains in the process of stretch-forming sheet metal. Int. J. Mech. Sci. 9, 609–620.

Meagher, T.F., 1964. The conversion of magnetic energy into shock pulses. ISA Trans. 3, 313.

Mercier, S., Molinari, A., 2003. Predictions of bifurcations and instabilities during dynamic extension. Int. J. Solids Struct. 40, 1995–2016.

Niordson, F.I., 1965. A unit for testing materials at high strain rates. Exp. Mech. 5, 29–32.

Pandolfi, A., Krysl, P., Ortiz, M., 1999. Finite element simulation of ring expansion and fragmentation: the capturing of length and time scales through cohesive models of fracture. Int. J. Fracture 95, 279–297.

Sorensen, N.J., Freund, L.B., 2000. Unstable neck formation in a ductile ring subjected to impulsive radial loading. Int. J. Solids Struct. 37, 2265–2283.

Yadav, S., Chichili, D.R., Ramesh, K.T., 1995. The mechanical response of a 6061-T6 Al/Al$_2$O$_3$ metal matrix composite at high rates of deformation. Acta Met. Mater. 43, 4453–4464.

Yadav, S., Repetto, E.A., Ravichandran, G., Ortiz, M., 2001. A computational study of the influence of thermal softening on ballistic penetration in metals. Intl. J. Impact Eng. 25, 787–803.